
Tractable Density Estimation on Learned Manifolds with Conformal Embedding Flows

Brendan Leigh Ross
Layer 6 AI
brendan@layer6.ai

Jesse C. Cresswell
Layer 6 AI
jesse@layer6.ai

Abstract

Normalizing flows are generative models that provide tractable density estimation by transforming a simple base distribution into a complex target distribution. However, this technique cannot directly model data supported on an unknown low-dimensional manifold, a common occurrence in real-world domains such as image data. Recent attempts to remedy this limitation have introduced geometric complications that defeat a central benefit of normalizing flows: exact density estimation. We recover this benefit with Conformal Embedding Flows, a framework for designing flows that learn manifolds with tractable densities. We argue that composing a standard flow with a trainable conformal embedding is the most natural way to model manifold-supported data. To this end, we present a series of conformal building blocks and apply them in experiments with real-world and synthetic data to demonstrate that flows can model manifold-supported distributions without sacrificing tractable likelihoods.

1 Introduction

Deep generative modelling is a rapidly evolving area of research in which the goal is to model a complex probability distribution from a set of samples. Research has been split between major approaches such as normalizing flows (NFs) [11, 42], generative adversarial networks (GANs) [16], variational autoencoders (VAEs) [26], energy-based models [13] and autoregressive models [36]. NFs in particular describe a distribution by modelling a change of variable function to a known base density. This approach provides the unique combination of efficient inference, efficient sampling, and exact likelihood estimation, but in practice generated images have not been as detailed or realistic as those of those of other methods [4, 6, 20, 23, 46].

One limiting aspect of traditional NFs is the use of a base density that has the same dimensionality as the data. This stands in contrast to models such as GANs and VAEs, which generate data by sampling from a low-dimensional latent prior and mapping the sample to data space. In many application domains, it is known or commonly assumed that the data of interest lives on a lower dimensional manifold embedded in the higher dimensional data space [14]. For example when modelling images, data samples belong to $[0, 1]^n$, where n is the number of pixels in each image and each pixel has a brightness in the domain $[0, 1]$. However, most points in this data space correspond to meaningless noise, whereas meaningful images of objects lie on an intrinsic manifold of dimension $m \ll n$. A traditional NF cannot take advantage of the lower dimensional nature of realistic images.

There is growing research interest in modifying flow-based generative models to incorporate a change in dimensionality between the base density and data space [3, 7, 8, 29, 28]. Flows from low-dimensional latent spaces to high-dimensional data spaces could benefit from making better use of fewer parameters, being more memory efficient, and could reveal information about the intrinsic structure of the data. Properties of the data manifold can be of interest as well, such as its dimensionality, or the semantic meaning of latent directions [26, 41]. However, leading approaches

to manifold-based flows still suffer from drawbacks including intractable density estimation [3] or reliance on stochastic inverses [8].

In this paper we propose Conformal Embedding Flows (CEFs), a class of flows that use *conformal embeddings* to transform from low to high dimensions while maintaining invertibility and an efficiently computable density. We show how conformal embeddings can be used to learn a lower dimensional data manifold, and we combine them with powerful NF architectures for learning densities. The overall CEF paradigm permits efficient density estimation, sampling, and inference. We propose several types of conformal embedding that can be implemented as composable layers of a flow, including a new invertible layer, the orthogonal $k \times k$ convolution. Lastly, we demonstrate their efficacy on synthetic and real-world data.

2 Background

2.1 Normalizing Flows

In the traditional setting of a normalizing flow [11, 42], a set of data points $\{\mathbf{x}_i\} \subset \mathcal{X} = \mathbb{R}^n$ treated as random samples from an unknown density $p_{\mathbf{x}}^*(\mathbf{x})$ is used to learn an approximate density $p_{\mathbf{x}}(\mathbf{x})$ via maximum likelihood estimation. The approximate density is modelled using a diffeomorphism $\mathbf{f} : \mathcal{Z} \rightarrow \mathcal{X}$ which maps a base density $p_{\mathbf{z}}(\mathbf{z})$ over the space $\mathcal{Z} = \mathbb{R}^n$, typically taken to be a multivariate normal, to $p_{\mathbf{x}}(\mathbf{x})$ via the change of variables formula

$$p_{\mathbf{x}}(\mathbf{x}) = p_{\mathbf{z}}(\mathbf{f}^{-1}(\mathbf{x})) |\det \mathbf{J}_{\mathbf{f}}(\mathbf{f}^{-1}(\mathbf{x}))|^{-1}, \quad (1)$$

where $\mathbf{J}_{\mathbf{f}}(\mathbf{z})$ is the Jacobian matrix of \mathbf{f} at the point \mathbf{z} . The change of variables formula derives from the principle of conservation of probability: the probability mass in an infinitesimal volume $d\mathbf{z}$ of \mathcal{Z} must be preserved in the volume of \mathcal{X} corresponding to the image $\mathbf{f}(d\mathbf{z})$, and it is exactly the Jacobian determinant that accounts for changes in the coordinate volume induced by \mathbf{f} . By parameterizing classes of diffeomorphisms \mathbf{f}_{θ} , the mapping can be learned with the maximum likelihood loss function for the sample set $\{\mathbf{x}_i\} \subset \mathcal{X}$. Altogether, the three following operations must be tractable: sampling with $\mathbf{f}(\mathbf{z})$, inference with $\mathbf{f}^{-1}(\mathbf{x})$, and density estimation with the $|\det \mathbf{J}_{\mathbf{f}}(\mathbf{z})|$ factor. To scale the model, one can compose many such layers $\mathbf{f} = \mathbf{f}_k \circ \dots \circ \mathbf{f}_1$, and the $|\det \mathbf{J}_{\mathbf{f}_i}(\mathbf{z})|$ factors multiply in Eq. (1).

Generally, there is no unifying way to parameterize an arbitrary bijection satisfying these constraints. Instead, normalizing flow research has progressed by designing new and more expressive component bijections which can be parameterized, learned, and composed. In particular, progress has been made by designing layers whose Jacobian determinants are tractable by construction. A significant theme has been to structure flows to have a triangular Jacobian [11, 42, 27, 12]. Kingma and Dhariwal [25] introduced invertible 1×1 convolution layers for image modelling; these produce block-diagonal Jacobians whose blocks are parameterized in a *PLU*-decomposition, so that the determinant can be computed in $\mathcal{O}(c)$, the number of input channels. See [38] for a thorough survey of normalizing flow models.

2.2 Injective Flows

The requirement that \mathbf{f} be a diffeomorphism fixes the dimensionality of the latent space. In turn, $p_{\mathbf{x}}(\mathbf{x})$ must have full support over \mathcal{X} , which is problematic when the data lies on a submanifold $\mathcal{M} \subset \mathcal{X}$ with dimension $m < n$. Dai and Wipf [9] observed that if a probability model with full support is fitted via maximum likelihood to such data, the estimated density can converge towards infinity on \mathcal{M} while ignoring the probability distribution of the data entirely. Behrmann et al. [2] point out that invertible neural networks can become numerically non-invertible, especially when the effective dimensionality of data and latents are mismatched. Correctly learning the data manifold along with its density may be able to circumvent these pathologies.

Injective flows seek to learn an explicitly low-dimensional support by reducing the dimensionality of the latent space and modelling the flow as a *smooth embedding*, or an injective function which is diffeomorphic to its image¹. This case can be accommodated with a generalized change of variables formula for densities as follows [15].

¹Throughout this work we use the term “embedding” in the topological sense of a function describing how a low-dimensional space sits as a manifold inside a high-dimensional space. This is not to be confused with other

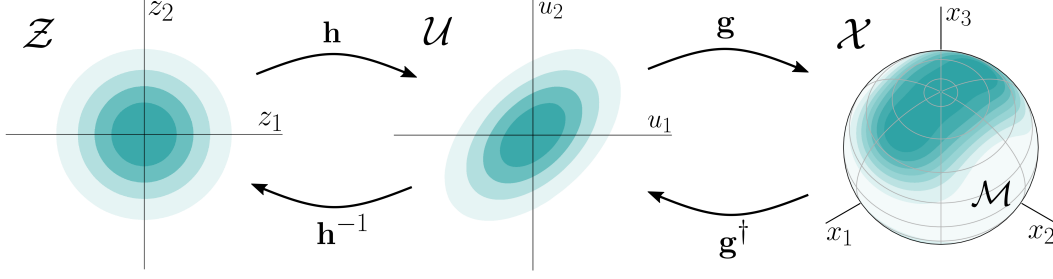


Figure 1: A normalized base density in the \mathcal{Z} space is mapped by a bijective flow \mathbf{h} to a more complicated density in \mathcal{U} . The injective component \mathbf{g} maps this density onto a manifold \mathcal{M} in \mathcal{X} . For inference, data points from \mathcal{M} follow the reverse path through \mathbf{g}^\dagger and \mathbf{h}^{-1} to the latent space where their likelihood can be evaluated, and combined with the determinant factors in Eq. (4).

Let $\mathbf{g} : \mathcal{U} \rightarrow \mathcal{X}$ be a smooth embedding from a latent space \mathcal{U} onto the data manifold $\mathcal{M} \subset \mathcal{X}$, that is, $\mathcal{M} = \mathbf{g}(\mathcal{U})$ is the range of \mathbf{g} . Since \mathbf{g} is a smooth embedding it has a left-inverse² $\mathbf{g}^\dagger : \mathcal{X} \rightarrow \mathcal{U}$ which is smooth on \mathcal{M} and satisfies $\mathbf{g}^\dagger(\mathbf{g}(\mathbf{u})) = \mathbf{u}$ for all $\mathbf{u} \in \mathcal{U}$. Suppose $p_{\mathbf{u}}(\mathbf{u})$ is a density on \mathcal{U} described using coordinates \mathbf{u} . The same density can be described in the ambient space \mathcal{X} using \mathbf{x} coordinates by pushing it through \mathbf{g} .

The quantity that accounts for changes in the coordinate volume at each point \mathbf{u} is $\sqrt{\det [\mathbf{J}_{\mathbf{g}}^T(\mathbf{u})\mathbf{J}_{\mathbf{g}}(\mathbf{u})]}$, where the Jacobian $\mathbf{J}_{\mathbf{g}}$ is now a $n \times m$ matrix [30]. Hence, using the shorthand $\mathbf{u} = \mathbf{g}^\dagger(\mathbf{x})$, the generalized change of variables formula defined for $\mathbf{x} \in \mathcal{M}$ can be written

$$p_{\mathbf{x}}(\mathbf{x}) = p_{\mathbf{u}}(\mathbf{u}) |\det [\mathbf{J}_{\mathbf{g}}^T(\mathbf{u})\mathbf{J}_{\mathbf{g}}(\mathbf{u})]|^{-\frac{1}{2}}. \quad (2)$$

While \mathbf{g} describes how the data manifold \mathcal{M} is embedded in the larger ambient space, the mapping \mathbf{g} alone may be insufficient to represent a normalized base density. As before, it is helpful to introduce a latent space \mathcal{Z} of dimension m along with a diffeomorphism $\mathbf{h} : \mathcal{Z} \rightarrow \mathcal{U}$ representing a bijective NF between \mathcal{Z} and \mathcal{U} [3]. Taking the overall injective transformation $\mathbf{g} \circ \mathbf{h}$ and applying the chain rule $\mathbf{J}_{\mathbf{g} \circ \mathbf{h}} = \mathbf{J}_{\mathbf{g}}\mathbf{J}_{\mathbf{h}}$ simplifies the determinant in Eq. (2) since the outer Jacobian $\mathbf{J}_{\mathbf{h}}$ is square,

$$\det [\mathbf{J}_{\mathbf{h}}^T \mathbf{J}_{\mathbf{g}}^T \mathbf{J}_{\mathbf{g}} \mathbf{J}_{\mathbf{h}}] = (\det \mathbf{J}_{\mathbf{h}})^2 \det [\mathbf{J}_{\mathbf{g}}^T \mathbf{J}_{\mathbf{g}}]. \quad (3)$$

Finally, writing $\mathbf{z} = \mathbf{h}^{-1}(\mathbf{u})$, the data density is modelled by

$$p_{\mathbf{x}}(\mathbf{x}) = p_{\mathbf{z}}(\mathbf{z}) |\det \mathbf{J}_{\mathbf{h}}(\mathbf{z})|^{-1} |\det [\mathbf{J}_{\mathbf{g}}^T(\mathbf{u})\mathbf{J}_{\mathbf{g}}(\mathbf{u})]|^{-\frac{1}{2}}, \quad (4)$$

with the entire process depicted in Fig.1.

Generating samples from $p_{\mathbf{x}}(\mathbf{x})$ is simple; a sample $\mathbf{z} \sim p_{\mathbf{z}}(\mathbf{z})$ is drawn from the base density and passed through $\mathbf{g} \circ \mathbf{h}$. Inference on a data sample $\mathbf{x} \sim p_{\mathbf{x}}(\mathbf{x})$ is achieved by passing it through $\mathbf{h}^{-1} \circ \mathbf{g}^\dagger$, evaluating the likelihood according to $p_{\mathbf{z}}(\mathbf{z})$, and computing both determinant factors.

Notably, the modeled density $p_{\mathbf{x}}(\mathbf{x})$ only has support on a low dimensional subset of \mathcal{X} , as per the manifold assumption for realistic data. In practice, though, there will be off-manifold points during training or if $\mathbf{g}(\mathbf{u})$ cannot perfectly fit the data, in which case the model’s log-likelihood will be $-\infty$. Cunningham et al. [8] remedy this by adding an off-manifold noise term to the model, but inference requires a stochastic inverse, and the model must be optimized using an ELBO-like objective. Other work [3, 5, 28] has projected data to the manifold via $\mathbf{g} \circ \mathbf{g}^\dagger$ prior to computing log-likelihoods, and optimized \mathbf{g} using the reconstruction loss $\mathbb{E}_{\mathbf{x} \sim p_{\mathbf{x}}} \|\mathbf{x} - \mathbf{g}(\mathbf{g}^\dagger(\mathbf{x}))\|^2$.

When computing log-likelihoods, the determinant term $\log \det [\mathbf{J}_{\mathbf{g}}^T \mathbf{J}_{\mathbf{g}}]$ presents a computational challenge. Kumar et al. [29] maximize it using an approximate lower bound, while Brehmer and Cranmer [3] and Kothari et al. [28] circumvent its computation altogether by only maximizing the

uses for the term in machine learning, namely a low-dimensional representation of high-dimensional or discrete data.

² \dagger denotes a left-inverse function, not necessarily the matrix pseudoinverse.

other terms in the log-likelihood. In concurrent work, Caterini et al. [5] optimize injective flows using a stochastic estimate of the log determinant. In line with research to build expressive bijective flows where $\det \mathbf{J}_f$ is tractable, our work focuses on designing and parameterizing injective flows where $\log \det [\mathbf{J}_g^T \mathbf{J}_g]$ as a whole is efficiently computable. In contrast to past injective flow models, our approach allows for straightforward evaluation and optimization of $\log \det [\mathbf{J}_g^T \mathbf{J}_g]$ in the same way standard NFs do for $\log |\det \mathbf{J}_f|$. As far as we can find, ours is the first approach to make this task tractable at scale.

3 Conformal Embedding Flows

In this section we propose Conformal Embedding Flows (CEFs) as a method for learning the low-dimensional manifold $\mathcal{M} \subset \mathcal{X}$ and the probability density of the data on the manifold.

Modern bijective flow work has produced tractable $\log |\det \mathbf{J}_f|$ terms by designing layers with triangular Jacobians [11, 12]. For injective flows, the combination $\mathbf{J}_g^T \mathbf{J}_g$ is symmetric, so it is triangular if and only if it is diagonal. In turn, $\mathbf{J}_g^T \mathbf{J}_g$ being diagonal is equivalent to \mathbf{J}_g having orthogonal columns. While this restriction is feasible for a single layer g , it is not composable. If g_1 and g_2 are both smooth embeddings whose Jacobians have orthogonal columns, it need not follow that $\mathbf{J}_{g_2 \circ g_1}$ has orthogonal columns. Additionally, since the Jacobians are not square, $\det [\mathbf{J}_{g_1}^T \mathbf{J}_{g_2}^T \mathbf{J}_{g_2} \mathbf{J}_{g_1}]$, the determinant in Eq. (2), cannot be factored into a product of individually computable terms as in Eq. (3). To ensure composability we propose enforcing the slightly more strict criteria that each $\mathbf{J}_g^T \mathbf{J}_g$ be a scalar multiple of the identity. This is precisely the condition that g is a conformal embedding.

Formally, $g : \mathcal{U} \rightarrow \mathcal{X}$ is a conformal embedding if it is a smooth embedding whose Jacobian satisfies

$$\mathbf{J}_g^T(\mathbf{u}) \mathbf{J}_g(\mathbf{u}) = \lambda^2(\mathbf{u}) \mathbf{I}_m, \quad (5)$$

where $\lambda : \mathcal{U} \rightarrow \mathbb{R}$ is a smooth non-zero scalar function, the *conformal factor* [30]. In other words, \mathbf{J}_g has orthonormal columns up to a non-zero multiplicative constant. Hence g locally preserves angles.

From Eq. (5) it is clear that conformal embeddings naturally satisfy our requirements as an injective flow. In particular, let $g : \mathcal{U} \rightarrow \mathcal{X}$ be a conformal embedding and $h : \mathcal{Z} \rightarrow \mathcal{U}$ be a standard normalizing flow model. The injective flow model $g \circ h : \mathcal{Z} \rightarrow \mathcal{X}$ satisfies

$$p_x(\mathbf{x}) = p_z(\mathbf{z}) |\det \mathbf{J}_h(\mathbf{z})|^{-1} \lambda^{-m}(\mathbf{u}). \quad (6)$$

We call $g \circ h$ a Conformal Embedding Flow.

There are multiple options for training a CEF. End-to-end maximum likelihood training could be used for $g \circ h$ as a whole, but when projecting to the manifold, it is possible to maximize density without learning the manifold correctly [3]. Without any initialization of g the model will struggle to isolate the data manifold \mathcal{M} as the range of g . We find it effective to first train the manifold learner g alone for several epochs by minimizing the reconstruction loss $\mathbb{E}_{\mathbf{x} \sim p_x^*} \|\mathbf{x} - g(g^\dagger(\mathbf{x}))\|^2$. After this manifold warmup phase, our model density can be optimized in two ways. The first way is the *sequential* training approach, in which we optimize h with g fixed as in Brehmer and Cranmer [3]. The alternative, which we refer to as the *joint* training approach, is to optimize the following loss,

$$\mathcal{L} = \mathbb{E}_{\mathbf{x} \sim p_x^*} [-\log p_x(\mathbf{x}) + \alpha \|\mathbf{x} - g(g^\dagger(\mathbf{x}))\|^2]. \quad (7)$$

This mixed loss is unique to our model because it is the first model for which $\log p_x(\mathbf{x})$ is tractable.

3.1 Designing Conformal Embedding Flows

In general, there is no unifying way to parameterize all conformal embeddings (See App. A for more discussion). Despite this, we can identify expressive classes of embeddings. For a conformal embedding g to be useful in a CEF we must be able to sample with $g(\mathbf{u})$, perform inference with $g^\dagger(\mathbf{x})$, and compute the conformal factor $\lambda(\mathbf{u})$. To build a parameterizable and scalable model g , it helps to work with conformal building blocks $g_i : \mathcal{U}_{i-1} \rightarrow \mathcal{U}_i$ (where $\mathcal{U}_0 = \mathcal{U}$ and $\mathcal{U}_k = \mathcal{X}$), which we compose to produce the full conformal embedding g :

$$g = g_k \circ \dots \circ g_1. \quad (8)$$

In turn, \mathbf{g} is conformal because

$$\mathbf{J}_{\mathbf{g}}^T \mathbf{J}_{\mathbf{g}} = (\mathbf{J}_{\mathbf{g}_1}^T \cdots \mathbf{J}_{\mathbf{g}_k}^T) (\mathbf{J}_{\mathbf{g}_k} \cdots \mathbf{J}_{\mathbf{g}_1}) = \lambda_1^2 \cdots \lambda_k^2 \mathbf{I}_m. \quad (9)$$

Our goal in the remainder of this section is to design classes of conformal building blocks which can be parameterized and learned in a CEF.

3.1.1 Conformal Embeddings from Conformal Mappings

Consider the special case where the conformal embedding maps between Euclidean spaces $\mathcal{U} \subseteq \mathbb{R}^d$ and $\mathcal{V} \subseteq \mathbb{R}^d$ of the same dimension³. In this special case \mathbf{g}_i is called a conformal mapping. Liouville’s theorem [18] states that any conformal mapping can be expressed as a composition of translations, orthogonal transformations, scalings, and inversions, which are defined in Table 1 (see App. A.1 for details on conformal mappings). We created conformal embeddings primarily by composing these layers. Zero-padding (which is trivially conformal) was interspersed to provide changes in dimensionality [3].

Table 1: Conformal Mappings

Type	Functional Form	Inverse	Conformal Factor $\lambda(\mathbf{u})$
Translation	$\mathbf{u} \mapsto \mathbf{u} + \mathbf{a}, \quad \mathbf{a} \in \mathbb{R}^d$	$\mathbf{v} \mapsto \mathbf{v} - \mathbf{a}$	1
Orthogonal	$\mathbf{u} \mapsto \mathbf{Q}\mathbf{u}, \quad \mathbf{Q} \in O(d)$	$\mathbf{v} \mapsto \mathbf{Q}^T \mathbf{v}$	1
Scaling	$\mathbf{u} \mapsto \lambda \mathbf{u}, \quad \lambda \in \mathbb{R}$	$\mathbf{v} \mapsto \lambda^{-1} \mathbf{v}$	λ
Inversion	$\mathbf{u} \mapsto \mathbf{u} / \ \mathbf{u}\ ^2,$	$\mathbf{v} \mapsto \mathbf{v} / \ \mathbf{v}\ ^2$	$\ \mathbf{u}\ ^{-2}$
SCT	$\mathbf{u} \mapsto \frac{\mathbf{u} - \ \mathbf{u}\ ^2 \mathbf{b}}{1 - 2\mathbf{b} \cdot \mathbf{u} + \ \mathbf{b}\ ^2 \ \mathbf{u}\ ^2}, \quad \mathbf{b} \in \mathbb{R}^d$	$\mathbf{v} \mapsto \frac{\mathbf{v} + \ \mathbf{v}\ ^2 \mathbf{b}}{1 + 2\mathbf{b} \cdot \mathbf{v} + \ \mathbf{b}\ ^2 \ \mathbf{v}\ ^2}$	$1 - 2\mathbf{b} \cdot \mathbf{u} + \ \mathbf{b}\ ^2 \ \mathbf{u}\ ^2$

Stacking translation, orthogonal transformation, scaling, and inversion layers is sufficient to learn any conformal mapping in principle. However, we found the inversion operation to be numerically unstable, so we replaced it with the *special conformal transformation* (SCT), a transformation of interest in conformal field theory [10]. It can be understood as an inversion, followed by a translation by $-\mathbf{b}$, followed by another inversion. In contrast to inversions, SCTs have a continuous parameter and include the identity when this parameter is set to 0.

The main challenge to achieving the full expressibility allowable within Liouville’s theorem is implementing trainable orthogonal layers. We parameterized orthogonal transformations in two different ways: by using Householder matrices [45], which are cheaply parameterizable and easy to train, and by using the API provided by [31], which parameterizes arbitrary orthogonal matrices with determinant 1 as the matrix exponential of a skew-symmetric matrix.

To scale orthogonal transformations to image data, we propose a new invertible layer: the orthogonal $k \times k$ convolution. In the spirit of the invertible 1×1 convolutions of Kingma and Dhariwal [25], we note that a $k \times k$ convolution with stride k has a block diagonal Jacobian. The Jacobian is orthogonal if and only if these blocks are orthogonal. It suffices then to convolve the input with a set of filters that together form an orthogonal matrix. It is also worth noting that these layers can be inverted efficiently by applying a transposed convolution with the same filter, while a standard invertible 1×1 convolution requires a matrix inversion. This facilitates quick forward and backward passes when optimizing the model’s reconstruction loss.

3.1.2 Piecewise Conformal Embeddings

To increase expressivity of the embeddings, the conformality condition on \mathbf{g} can be relaxed to the point of being conformal *almost everywhere*. Formally, the latent spaces \mathcal{Z} and \mathcal{U} are redefined as $\mathcal{Z} = \{\mathbf{z} : \mathbf{g} \text{ is conformal at } \mathbf{h}(\mathbf{z})\}$ and $\mathcal{U} = \mathbf{h}(\mathcal{Z})$. Then \mathbf{g} remains a conformal embedding on \mathcal{U} , and as long as $\{\mathbf{x} : \mathbf{g} \text{ is nonconformal at } \mathbf{g}^\dagger(\mathbf{x})\}$ also has measure zero, this approach poses no practical problems. Note that the same relaxation is performed implicitly with the diffeomorphism property of standard flows when rectifier nonlinearities are used in coupling layers [12].

³We consider conformal mappings between spaces of dimension $d > 2$. Conformal mappings in $d = 2$ are much less constrained, while the case $d = 1$ is trivial since there is no notion of an angle.

Table 2: Piecewise Conformal Embeddings

Type	Functional Form	Left-Inverse	$\lambda(\mathbf{u})$
Conformal ReLU [28]	$\mathbf{u} \mapsto \text{ReLU} \begin{bmatrix} \mathbf{Q}\mathbf{u} \\ -\mathbf{Q}\mathbf{u} \end{bmatrix}, \quad \mathbf{Q} \in O(d)$	$\begin{bmatrix} \mathbf{v}_1 \\ \mathbf{v}_2 \end{bmatrix} \mapsto \mathbf{Q}^T (\mathbf{v}_1 - \mathbf{v}_2)$	1
Conditional Orthogonal	$\mathbf{u} \mapsto \begin{cases} \mathbf{Q}_1\mathbf{u} & \text{if } \ \mathbf{u}\ < 1 \\ \mathbf{Q}_2\mathbf{u} & \text{if } \ \mathbf{u}\ \geq 1 \end{cases}, \quad \mathbf{Q}_1, \mathbf{Q}_2 \in O(d)$	$\mathbf{v} \mapsto \begin{cases} \mathbf{Q}_1^T\mathbf{u} & \text{if } \ \mathbf{v}\ < 1 \\ \mathbf{Q}_2^T\mathbf{u} & \text{if } \ \mathbf{v}\ \geq 1 \end{cases}$	1

We considered the two piecewise conformal embeddings defined in Table 2. Due to the success of ReLU in standard deep neural networks [35], we try a ReLU-like layer that is piecewise conformal. *Conformal ReLU* is based on the injective ReLU proposed by Kothari et al. [28]. We believe it to be of general interest as a conformal nonlinearity, but it provided no performance improvements in our experiments. More useful was the *Conditional Orthogonal* transformation, which takes advantage of the norm-preservation of orthogonal transformations to create an invertible layer. Despite the Conditional Orthogonal layer being discontinuous, it provided a substantial boost in reconstruction ability on image data.

4 Related Work

Flows on prescribed manifolds Flows can be developed for Riemannian manifolds $\mathcal{M} \subseteq \mathcal{X}$ which are known in advance and can be defined as the image of some fixed $\phi : \mathcal{U} \rightarrow \mathcal{X}$, where $\mathcal{U} \subseteq \mathbb{R}^m$ [15, 34, 38]. In particular, Rezende et al. [43] model densities on spheres and tori with convex combinations of Möbius transformations, which are cognate to conformal mappings. For known manifolds ϕ is fixed, and the density’s log Jacobian determinant term may be computable in closed form. Our work replaces ϕ with a trainable network g , but the log Jacobian determinant still has a simple closed form.

Flows on learnable manifolds Extending flows to learnable manifolds brings about two main challenges: handling off-manifold points, and training the density on the manifold.

If the manifold is the density’s support, all off-manifold points during training will have a likelihood of 0. This has been addressed by adding an off-manifold noise term [8, 7] or by training the manifold with a reconstruction loss and projecting the data onto the manifold [3, 28, 29]. We opt for the latter approach.

Training the density on the manifold is challenging because the log-determinant term is typically intractable. Kumar et al. [29] use a series of lower bounds to train the log-determinant, while Brehmer and Cranmer [3] and Kothari et al. [28] separate the flow into two components, and only train the low-dimensional part of the flow. Caterini et al. [5] are able to maximize log-likelihood directly using a stochastic approximation of the flow’s log-determinant, which allows for a fully expressive invertible model as the embedding component, but remains computationally expensive for high dimensional data. Our approach is the first injective model to provide a learnable manifold with exact log-determinant computation.

Conformal networks Numerous past works have imposed approximate conformality or its special cases as a regularizer [1, 22, 39, 40, 47], but it has been less common to enforce conformality strictly. To maintain orthogonal weights, one must optimize along the *Stiefel manifold* of orthogonal matrices. Past work to achieve this has either trained with Riemannian gradient descent or directly parameterized subsets of orthogonal matrices. Riemannian gradient descent algorithms typically require a singular value or QR decomposition at each training step [17, 21, 37]. We found that directly parameterizing orthogonal matrices to train more quickly. In particular, Lezcano-Casado and Martínez-Rubio [32] and Lezcano-Casado [31] parameterize orthogonal matrices as the matrix exponential of a skew-symmetric matrix, and Tomczak and Welling [45] use Householder matrices. We used a mix of both.

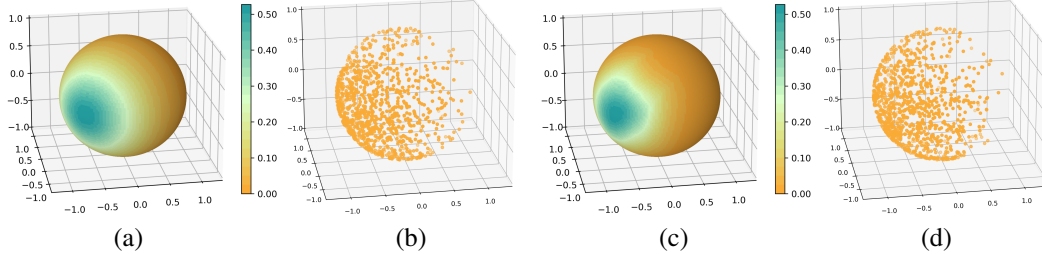


Figure 2: (a) A density $p_{\mathbf{x}}^*(\mathbf{x})$ with support on the sphere, and (b) 10^3 samples comprising the training dataset $\{\mathbf{x}_i\}$. (c) The density learned by a CEF, and (d) 10^3 generated samples.

5 Experiments

5.1 Synthetic Spherical Data

To demonstrate how a CEF can jointly learn a manifold and density, we generated a synthetic dataset from a known distribution with support on a spherical surface embedded in \mathbb{R}^3 as described in App. B. The distribution is visualized in Fig. 2, along with the training dataset of 10^3 sampled points.

Since the manifold dimension is known, we constructed a simple \mathbf{g} for learning the manifold composed from a padding layer, and the conformal mappings in Table 1. The bijective component \mathbf{h} for density normalization consisted of three sets of Glow-style steps of {ActNorm, invertible 1×1 convolution, affine coupling} acting on the two latent dimensions as channels.

We trained the two components of the CEF jointly, with a reconstruction loss initialization phase for \mathbf{g} , followed by the mixed loss function in Eq. (7) with an end-to-end log-likelihood term. The resulting model density is plotted in Fig. 2 along with generated samples, and shows good fidelity to the known manifold and density.

5.2 Image Modelling

We scale CEFs to larger data by training on the CelebA dataset for which a low-dimension manifold structure is postulated but not known [33]⁴. Our aim is to show that, despite restricting its functional form to provide exact likelihood estimation, CEFs are competitive with mainstream injective flow training approaches [3, 28]. In doing so, we are the first to perform end-to-end maximum likelihood training with an injective flow on image data. Three approaches were evaluated: a sequentially trained baseline model, a sequentially trained CEF, and a jointly trained CEF. We fixed a small Glow-style stump with 3 levels and 3 steps per level as the backbone \mathbf{h} for all models.

The baseline’s embedding \mathbf{g} is a Glow-style network of 3 levels and 2 steps per level: the output of each scale is reshaped into 8×8 , and all scales are concatenated. We then apply an invertible 1×1 convolution, and project the input down to 1536 dimensions. Since this network is not conformal, joint training is intractable, so it must be trained sequentially. On the other hand, both CEFs use the same conformal architecture for \mathbf{g} : a series of 2×2 and 1×1 Householder convolutions interspersed with Conditional Orthogonal convolutions, padding layers, shifts, and scales. All models were trained with the Adam optimizer [24] with learning rate 1×10^{-5} for 100 epochs. Using a single NVIDIA TITAN V, the sequential baseline and sequential CEF ran for 34 hours, while the joint CEF ran for 65 hours. More experimental details are provided in App. B.

Injective models cannot be compared on the basis of log-likelihood, since each model may have a different manifold support. Instead, we compare images on the basis of FID score [19], of which the mean and standard deviation is computed for each model over 3 sets of generated samples. We use the popular PyTorch-FID package [44]. As expected, since the baseline embedding is more flexible, it achieves smaller reconstruction losses than the conformal models. However, the CEFs produce competitive FID scores, possibly due to the better global consistency of facial features from the two CEF models. In contrast, the baseline model learns locally sharp features, but more amorphous faces.

⁴The CelebA dataset is available for non-commercial research purposes only. For specifics please refer to the CelebA website.

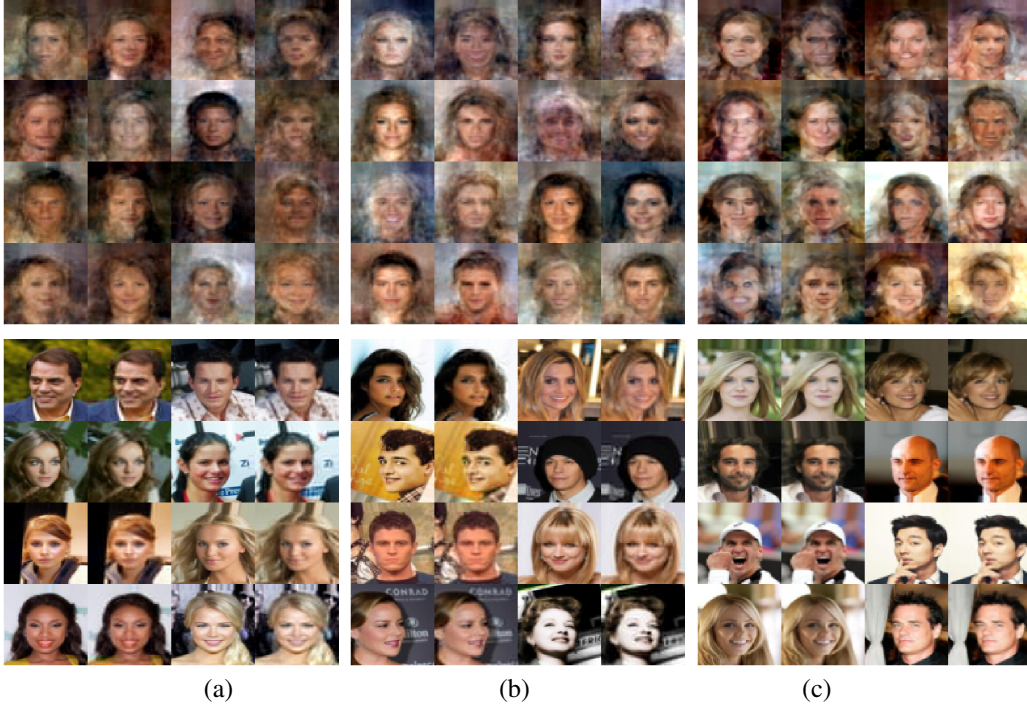


Figure 3: Generated samples (top) and reconstructions (bottom) for (a) the jointly trained CEF, (b) the sequentially trained CEF, and (c) the sequentially trained baseline model. In the reconstruction panes, original images are shown on the left, while reconstructions are shown on the right.

We hypothesize that the conformally embedded manifold creates a simpler optimization surface, so the stump picks up on global symmetries more easily.

Table 3: CelebA Performance

Approach	FID	Reconstruction	$\mathbf{g} + \mathbf{h}$ Parameters
Sequential Baseline	110.87 ± 0.12	0.402×10^{-3}	$36346752 + 36429778$
Sequential CEF	111.76 ± 0.14	1.046×10^{-3}	$83036 + 36429778$
Joint CEF	126.04 ± 0.23	1.043×10^{-3}	$83036 + 36429778$

6 Limitations and Future Directions

Expressivity Just as standard flows trade some expressibility for tractable likelihoods, so must injective flows. Our conformal networks in particular are less expressive than state-of-the-art flow models; for instance, our model produced blurry reconstructions of CelebA data when the latent dimension was below 1000, while Brehmer and Cranmer [3] use a latent dimension of 512. We mostly compose padding layers and dimension-*preserving* conformal mappings, which is a naturally restrictive class by Liouville’s theorem [18]. Just as early work on NFs [11, 42] introduced limited classes of parameterizable bijections, which were later improved in many directions, our work introduces several classes of parameterizable conformal embeddings. We expect that future work will uncover more expressive dimension-*increasing* conformal embeddings.

Manifold Learning Strictly manifold-supported probability models such as ours introduce a bi-objective optimization problem. How to balance these objectives is unclear and, thus far, empirical [3]. The difference in supports between two manifold models also makes their likelihoods incomparable. Cunningham et al. [8] have made progress in this direction by adding noise to data generated on the manifold, but this makes inversion stochastic and introduces density estimation challenges. We

suspect that using conformal manifold-learners may make density estimation more tractable in this setting, but further research is needed in this direction.

Dataset bias and consent Clearly, the CelebA dataset does not accurately represent the real-world distribution of human traits. Models trained on CelebA, and indeed any other possibly biased datasets, should be vetted for fairness before being deployed to make decisions that can adversely affect human beings. Intuitively, manifold-learning as a task should be robust to mild dataset biases, hence capturing underrepresented segments of a population better than standard generative models, but this has yet to be formalized or experimentally validated. We also note that while the human subjects in these images are all public figures, they may not have explicitly provided consent for their images to be used for research purposes.

7 Conclusion

In this paper, we introduced Conformal Embedding Flows for modelling probability distributions on low-dimensional manifolds while maintaining tractable densities. We showed that conformal embeddings naturally fit the framework of injective flows by providing fast sampling, invertibility for inference, and a simple Jacobian determinant factor for efficient likelihood estimation, all while being composable for scaling to deep models. Furthermore, the restrictions on conformal embeddings are minimal, in that any looser condition will sacrifice one or more of these properties. As we have reviewed, previous works on injective flows do not maintain all of these properties simultaneously.

Normalizing flows are still outperformed by other generative models such as GANs and VAEs in the arena of realistic image generation. Notably, these two alternatives benefit from a low-dimensional latent space, which better reflects image data’s manifold structure and provides for more scalable model design. By equipping flows with a low-dimensional latent space, injective flow models have made progress towards achieving VAE- or GAN-level performance. The CEF paradigm is a way to match these strides while maintaining the theoretical strengths of NFs.

Broader Impact Natural image generation is a common task in generative modelling, with human face datasets frequently used as benchmarks for model performance. However, there are concerns that highly realistic generated images could be used for unethical purposes such as fraud. Our work is primarily focused on the theoretical properties of flow models, not on generating highly realistic images. As more powerful approaches already exist for realistic image generation [4, 23, 46, 6], our research is unlikely to lead to any broader impact on society in terms of unethical use of image generation.

Acknowledgments and Disclosure of Funding

We would like to thank Gabriel Loaiza-Ganem and Anthony Caterini for their discussions and advice. We would also like to thank Parsa Torabian for sharing his experience with orthogonal models, and Maksims Volkovs for his comments and advice.

References

- [1] N. Bansal, X. Chen, and Z. Wang. Can We Gain More from Orthogonality Regularizations in Training Deep Networks? In *Advances in Neural Information Processing Systems*, volume 31, 2018.
- [2] J. Behrmann, P. Vicol, K.-C. Wang, R. Grosse, and J.-H. Jacobsen. Understanding and mitigating exploding inverses in invertible neural networks. In *Proceedings of The 24th International Conference on Artificial Intelligence and Statistics*, volume 130, pages 1792–1800. PMLR, 13–15 Apr 2021.
- [3] J. Brehmer and K. Cranmer. Flows for simultaneous manifold learning and density estimation. In *Advances in Neural Information Processing Systems*, volume 33, 2020.
- [4] A. Brock, J. Donahue, and K. Simonyan. Large scale GAN training for high fidelity natural image synthesis. In *International Conference on Learning Representations*, 2019.

- [5] A. L. Caterini, G. Loaiza-Ganem, G. Pleiss, and J. P. Cunningham. Rectangular flows for manifold learning. *arXiv:2106.01413*, 2021.
- [6] R. Child. Very deep VAEs generalize autoregressive models and can outperform them on images. In *International Conference on Learning Representations*, 2021.
- [7] E. Cunningham and M. Fiterau. A change of variables method for rectangular matrix-vector products. In *Proceedings of The 24th International Conference on Artificial Intelligence and Statistics*, volume 130. PMLR, 2021.
- [8] E. Cunningham, R. Zabounidis, A. Agrawal, I. Fiterau, and D. Sheldon. Normalizing Flows Across Dimensions. *arXiv:2006.13070*, 2020.
- [9] B. Dai and D. Wipf. Diagnosing and Enhancing VAE Models. In *International Conference on Learning Representations, ICLR 2019*, 2019.
- [10] P. Di Francesco, P. Mathieu, and D. Sénéchal. *Conformal field theory*. Springer Science & Business Media, 2012.
- [11] L. Dinh, D. Krueger, and Y. Bengio. Nice: Non-linear independent components estimation. *arXiv:1410.8516*, 2014.
- [12] L. Dinh, J. Sohl-Dickstein, and S. Bengio. Density estimation using Real NVP. In *International Conference on Learning Representations, ICLR 2017*, 2017.
- [13] Y. Du and I. Mordatch. Implicit generation and modeling with energy based models. In H. Wallach, H. Larochelle, A. Beygelzimer, F. d'Alché-Buc, E. Fox, and R. Garnett, editors, *Advances in Neural Information Processing Systems*, volume 32, 2019.
- [14] C. Fefferman, S. Mitter, and H. Narayanan. Testing the manifold hypothesis. *Journal of the American Mathematical Society*, 29(4):983–1049, 2016.
- [15] M. C. Gemici, D. Rezende, and S. Mohamed. Normalizing Flows on Riemannian Manifolds, 2016.
- [16] I. J. Goodfellow, J. Pouget-Abadie, M. Mirza, B. Xu, D. Warde-Farley, S. Ozair, A. Courville, and Y. Bengio. Generative adversarial networks. *arXiv:1406.2661*, 2014.
- [17] M. Harandi and B. Fernando. Generalized BackPropagation, Étude De Cas: Orthogonality. *arXiv:1611.05927*, 2016.
- [18] P. Hartman. On isometries and on a theorem of Liouville. *Mathematische Zeitschrift*, 69: 202–210, 1958.
- [19] M. Heusel, H. Ramsauer, T. Unterthiner, B. Nessler, and S. Hochreiter. GANs Trained by a Two Time-Scale Update Rule Converge to a Local Nash Equilibrium. In *Advances in Neural Information Processing Systems*, volume 30, 2017.
- [20] J. Ho, A. Jain, and P. Abbeel. Denoising diffusion probabilistic models. In *Advances in Neural Information Processing Systems*, volume 33, pages 6840–6851, 2020.
- [21] L. Huang, X. Liu, B. Lang, A. W. Yu, and B. Li. Orthogonal weight normalization: Solution to optimization over multiple dependent stiefel manifolds in deep neural networks. In *AAAI*, 2018.
- [22] K. Jia, D. Tao, S. Gao, and X. Xu. Improving training of deep neural networks via singular value bounding. In *2017 IEEE Conference on Computer Vision and Pattern Recognition (CVPR)*, pages 3994–4002, 2017.
- [23] T. Karras, S. Laine, and T. Aila. A style-based generator architecture for generative adversarial networks. In *Proceedings of the IEEE/CVF Conference on Computer Vision and Pattern Recognition (CVPR)*, June 2019.
- [24] D. P. Kingma and J. Ba. Adam: A method for stochastic optimization. In *ICLR (Poster)*, 2015. URL <http://arxiv.org/abs/1412.6980>.

- [25] D. P. Kingma and P. Dhariwal. Glow: Generative Flow with Invertible 1x1 Convolutions. In *Advances in Neural Information Processing Systems*, volume 31, 2018.
- [26] D. P. Kingma and M. Welling. Auto-encoding Variational Bayes. *arXiv:1312.6114*, 2013.
- [27] D. P. Kingma, T. Salimans, R. Jozefowicz, X. Chen, I. Sutskever, and M. Welling. Improved variational inference with inverse autoregressive flow. In *Advances in Neural Information Processing Systems*, volume 29, 2016.
- [28] K. Kothari, A. Khorashadizadeh, M. de Hoop, and I. Dokmanić. Trumpets: Injective Flows for Inference and Inverse Problems. *arxiv:2102.10461*, 2021.
- [29] A. Kumar, B. Poole, and K. Murphy. Regularized Autoencoders via Relaxed Injective Probability Flow. In *Proceedings of the Twenty Third International Conference on Artificial Intelligence and Statistics*, volume 108, pages 4292–4301, 2020.
- [30] J. M. Lee. *Introduction to Riemannian manifolds*. Springer, 2018.
- [31] M. Lezcano-Casado. Trivializations for gradient-based optimization on manifolds. In *Advances in Neural Information Processing Systems, NeurIPS*, pages 9154–9164, 2019.
- [32] M. Lezcano-Casado and D. Martínez-Rubio. Cheap Orthogonal Constraints in Neural Networks: A Simple Parametrization of the Orthogonal and Unitary Group. In *Proceedings of the 36th International Conference on Machine Learning*, volume 97, pages 3794–3803, 2019.
- [33] Z. Liu, P. Luo, X. Wang, and X. Tang. Deep learning face attributes in the wild. In *Proceedings of International Conference on Computer Vision (ICCV)*, December 2015.
- [34] E. Mathieu and M. Nickel. Riemannian Continuous Normalizing Flows. In *Advances in Neural Information Processing Systems*, volume 33, pages 2503–2515, 2020.
- [35] V. Nair and G. E. Hinton. Rectified linear units improve restricted boltzmann machines. In *Proceedings of the 27th International Conference on International Conference on Machine Learning, ICML’10*, page 807–814, 2010.
- [36] A. V. Oord, N. Kalchbrenner, and K. Kavukcuoglu. Pixel recurrent neural networks. In *Proceedings of The 33rd International Conference on Machine Learning*, volume 48 of *Proceedings of Machine Learning Research*, pages 1747–1756. PMLR, 2016.
- [37] M. Ozay and T. Okatani. Optimization on Submanifolds of Convolution Kernels in CNNs. *arXiv: 1610.07008*, 2016.
- [38] G. Papamakarios, E. Nalisnick, D. J. Rezende, S. Mohamed, and B. Lakshminarayanan. Normalizing Flows for Probabilistic Modeling and Inference. *Journal of Machine Learning Research*, 22(57):1–64, 2021.
- [39] E. Peterfreund, O. Lindenbaum, F. Dietrich, T. Bertalan, M. Gavish, I. G. Kevrekidis, and R. R. Coifman. Local conformal autoencoder for standardized data coordinates. *Proceedings of the National Academy of Sciences*, 117(49):30918–30927, 2020.
- [40] H. Qi, C. You, X. Wang, Y. Ma, and J. Malik. Deep isometric learning for visual recognition. In *Proceedings of the 37th International Conference on Machine Learning*, volume 119, pages 7824–7835, 2020.
- [41] A. Radford, L. Metz, and S. Chintala. Unsupervised Representation Learning with Deep Convolutional Generative Adversarial Networks. In *International Conference on Learning Representations*, 2016.
- [42] D. Rezende and S. Mohamed. Variational Inference with Normalizing Flows. In *Proceedings of the 32nd International Conference on Machine Learning*, volume 37, pages 1530–1538, 2015.
- [43] D. J. Rezende, G. Papamakarios, S. Racaniere, M. Albergo, G. Kanwar, P. Shanahan, and K. Cranmer. Normalizing Flows on Tori and Spheres. In *Proceedings of the 37th International Conference on Machine Learning*, volume 119, pages 8083–8092, 2020.

- [44] M. Seitzer. pytorch-fid: FID Score for PyTorch. <https://github.com/mseitzer/pytorch-fid>, August 2020. Version 0.1.1.
- [45] J. M. Tomczak and M. Welling. Improving Variational Auto-Encoders using Householder Flow. *arXiv: 1611.09630*, 2016.
- [46] A. Vahdat and J. Kautz. NVAE: A Deep Hierarchical Variational Autoencoder. In *Advances in Neural Information Processing Systems*, volume 33, pages 19667–19679, 2020.
- [47] L. Xiao, Y. Bahri, J. Sohl-Dickstein, S. Schoenholz, and J. Pennington. Dynamical isometry and a mean field theory of CNNs: How to train 10,000-layer vanilla convolutional neural networks. In *Proceedings of the 35th International Conference on Machine Learning*, volume 80, pages 5393–5402, 2018.

A Details on Conformal Embeddings and Conformal Mappings

Let $(\mathcal{U}, \eta_{\mathbf{u}})$ and $(\mathcal{X}, \eta_{\mathbf{x}})$ be two Riemannian manifolds. We define a diffeomorphism $\mathbf{f} : \mathcal{U} \rightarrow \mathcal{X}$ to be a *conformal diffeomorphism* if it pulls back the metric $\eta_{\mathbf{x}}$ to be some non-zero scalar multiple of $\eta_{\mathbf{u}}$ [30]. That is,

$$\mathbf{f}^* \eta_{\mathbf{x}} = \lambda \eta_{\mathbf{u}} \quad (10)$$

for some smooth scalar function $\lambda \neq 0$. Many authors require λ to be positive, but we allow it to be negative. Furthermore, we define a smooth embedding $\mathbf{g} : \mathcal{U} \rightarrow \mathcal{X}$ to be a *conformal embedding* if it is a conformal diffeomorphism onto its image $(\mathbf{g}(\mathcal{U}), \eta_{\mathbf{x}})$, where $\eta_{\mathbf{x}}$ is inherited from the ambient space \mathcal{X} .

In our context, $\mathcal{U} \subseteq \mathbb{R}^m$, $\mathcal{X} = \mathbb{R}^n$, and $\eta_{\mathbf{u}}$ and $\eta_{\mathbf{x}}$ are Euclidean metrics. This leads to an equivalent property (Eq. (5)):

$$\mathbf{J}_{\mathbf{g}}^T(\mathbf{u}) \mathbf{J}_{\mathbf{g}}(\mathbf{u}) = \lambda^2(\mathbf{u}) \mathbf{I}_m. \quad (11)$$

This also guarantees that $\det[\mathbf{J}_{\mathbf{g}}^T \mathbf{J}_{\mathbf{g}}] = \lambda^{2m}$ is tractable, even when $\mathbf{g} = \mathbf{g}_k \circ \dots \circ \mathbf{g}_1$ is composed from several layers, as is needed for scalable injective flows.

To demonstrate that conformal embeddings are an expressive class of functions, we first turn to the most restricted case where $n = m$; i.e. conformal mappings. In Apps. A.1 and A.2 we provide an intuitive investigation of the classes of conformal mappings using infinitesimals. We then discuss in App. A.3 why conformal embeddings in general are more challenging to analyze, but also show intuitively why they are more expressive than dimension-preserving conformal mappings.

A.1 Infinitesimal Conformal Mappings

Consider a mapping of Euclidean space with dimension $m \geq 3$. Liouville’s theorem for conformal mappings constrains the set of such maps which satisfy the conformal condition Eq. (11). Such functions can be decomposed into translations, orthogonal transformations, scalings, and inversions. Here we provide a direct approach for the interested reader, which also leads to some insight on the general case of conformal embeddings [10]. First we will find all infinitesimal transformations which satisfy the conformal condition, then exponentiate them to obtain the set of finite conformal mappings.

Consider a transformation $\mathbf{f} : \mathbb{R}^m \rightarrow \mathbb{R}^m$ which is infinitesimally close to the identity function, expressed in Cartesian coordinates as

$$\mathbf{f}(\mathbf{x}) = \mathbf{x} + \boldsymbol{\epsilon}(\mathbf{x}). \quad (12)$$

That is, we only keep terms linear in the infinitesimal quantity $\boldsymbol{\epsilon}$. The mappings produced will only encompass transformations which are continuously connected to the identity, but we restrict our attention to these for now. However, this simple form allows us to directly study how Eq. (11) constrains the infinitesimal $\boldsymbol{\epsilon}(\mathbf{x})$:

$$\begin{aligned} \mathbf{J}_{\mathbf{f}}^T(\mathbf{x}) \mathbf{J}_{\mathbf{f}}(\mathbf{x}) &= \left[\mathbf{I}_m + \frac{\partial \boldsymbol{\epsilon}}{\partial \mathbf{x}} \right]^T \left[\mathbf{I}_m + \frac{\partial \boldsymbol{\epsilon}}{\partial \mathbf{x}} \right] \\ &= \mathbf{I}_m + \frac{\partial \boldsymbol{\epsilon}^T}{\partial \mathbf{x}} + \frac{\partial \boldsymbol{\epsilon}}{\partial \mathbf{x}}. \end{aligned} \quad (13)$$

By Eq. (11), the symmetric sum of $\partial \boldsymbol{\epsilon} / \partial \mathbf{x}$ must be proportional to the identity matrix. Let us call the position-dependent proportionality factor $\eta(\mathbf{x})$. We can start to understand $\eta(\mathbf{x})$ by taking a trace

$$\frac{\partial \boldsymbol{\epsilon}^T}{\partial \mathbf{x}} + \frac{\partial \boldsymbol{\epsilon}}{\partial \mathbf{x}} = \eta(\mathbf{x}) \mathbf{I}_m, \quad (14)$$

$$\frac{2}{m} \text{tr} \left(\frac{\partial \boldsymbol{\epsilon}}{\partial \mathbf{x}} \right) = \eta(\mathbf{x}). \quad (15)$$

Taking another derivative of Eq. (14) proves to be useful, so we switch to index notation to handle the tensor multiplications,

$$\frac{\partial}{\partial x_k} \frac{\partial \epsilon_j}{\partial x_i} + \frac{\partial}{\partial x_k} \frac{\partial \epsilon_i}{\partial x_j} = \frac{\partial \eta}{\partial x_k} \delta_{ij}, \quad (16)$$

where the Kronecker delta δ_{ij} is 1 if $i = j$, and 0 otherwise. On the left-hand-side, derivatives can be commuted. By taking a linear combination of the three permutations of indices we come to

$$2 \frac{\partial}{\partial x_k} \frac{\partial \epsilon_i}{\partial x_j} = \frac{\partial \eta}{\partial x_j} \delta_{ik} + \frac{\partial \eta}{\partial x_k} \delta_{ij} - \frac{\partial \eta}{\partial x_i} \delta_{jk}. \quad (17)$$

Summing over elements where $j = k$ gives the Laplacian of ϵ_i , while picking up only the derivatives of η with respect to x_i , so we can switch back to vector notation where

$$2 \nabla^2 \epsilon = (2 - m) \frac{\partial \eta}{\partial \mathbf{x}}. \quad (18)$$

Now we have two equations (14) and (18)⁵ involving derivatives of ϵ and η . To eliminate ϵ , we can apply ∇^2 to (14), while applying $\partial/\partial \mathbf{x}$ to (18)

$$\nabla^2 \frac{\partial \epsilon}{\partial \mathbf{x}}^T + \nabla^2 \frac{\partial \epsilon}{\partial \mathbf{x}} = \nabla^2 \eta \mathbf{I}_d \quad (19)$$

$$2 \nabla^2 \frac{\partial \epsilon}{\partial \mathbf{x}} = (2 - m) \frac{\partial^2 \eta}{\partial \mathbf{x} \partial \mathbf{x}}. \quad (20)$$

Since Eq. (20) is manifestly symmetric, the left-hand-sides are actually equal. Equating the right-hand-sides, we can again sum the diagonal terms, giving the much simpler form

$$(m - 1) \nabla^2 \eta = 0. \quad (21)$$

Ultimately, revisiting Eq. (20) shows that the function $\eta(\mathbf{x})$ is linear in the coordinates

$$\frac{\partial^2 \eta}{\partial \mathbf{x} \partial \mathbf{x}} = 0 \implies \eta(\mathbf{x}) = \alpha + \beta \cdot \mathbf{x}, \quad (22)$$

for constants α, β . This allows us to relate back to the quantity of interest ϵ . Skimming back over the results so far, the most general equation where having the linear expression for $\eta(\mathbf{x})$ helps is Eq. (17) which now is

$$2 \frac{\partial}{\partial x_k} \frac{\partial \epsilon_i}{\partial x_j} = \beta_j \delta_{ik} + \beta_k \delta_{ij} - \beta_i \delta_{jk}. \quad (23)$$

The point is that the right-hand-side is constant, meaning that $\epsilon(\mathbf{x})$ is at most quadratic in \mathbf{x} . Hence, we can make an ansatz for ϵ in full generality, involving sets of infinitesimal constants

$$\epsilon = \mathbf{a} + \mathbf{B}\mathbf{x} + \mathbf{x} \vec{\mathbf{C}} \mathbf{x}, \quad (24)$$

where $\vec{\mathbf{C}} \in \mathbb{R}^{m \times m \times m}$ is a 3-tensor.

So far we have found that infinitesimal conformal transformations can have at most quadratic dependence on the coordinates. It remains to determine the constraints on each set of constants \mathbf{a} , \mathbf{B} , and $\vec{\mathbf{C}}$, and interpret the corresponding mappings. We consider each of them in turn.

All constraints on ϵ involve derivatives, so there is nothing more to say about the constant term. It represents an infinitesimal translation

$$\mathbf{f}(\mathbf{x}) = \mathbf{x} + \mathbf{a}. \quad (25)$$

On the other hand, the linear term is constrained by Eqs. (14) and (15) which give

$$\mathbf{B} + \mathbf{B}^T = \frac{2}{m} \text{tr}(\mathbf{B}) \mathbf{I}_m. \quad (26)$$

Hence, \mathbf{B} has an unconstrained anti-symmetric part $\mathbf{B}_{\text{AS}} = \frac{1}{2}(\mathbf{B} - \mathbf{B}^T)$ representing an infinitesimal rotation

$$\mathbf{f}(\mathbf{x}) = \mathbf{x} + \mathbf{B}_{\text{AS}} \mathbf{x}, \quad (27)$$

⁵We note that the steps following Eq. (18) are only justified for $m \geq 3$ which we have assumed. In two dimensions the conformal group is much larger and Liouville's theorem no longer captures all conformal mappings.

while its symmetric part is diagonal as in Eq. (26),

$$\mathbf{f}(\mathbf{x}) = \mathbf{x} + \lambda \mathbf{x}, \quad \lambda = \frac{1}{m} \text{tr}(\mathbf{B}), \quad (28)$$

which is an infinitesimal scaling. This leaves only the quadratic term for interpretation which is more easily handled in index notation, i.e. $\epsilon_i = \sum_{lm} C_{ilm} x_l x_m$. The quadratic term is significantly restricted by Eq. (23),

$$2 \frac{\partial^2}{\partial x_k \partial x_j} \sum_{lm} C_{ilm} x_l x_m = 2C_{ijk} = \beta_j \delta_{ik} + \beta_k \delta_{ij} - \beta_i \delta_{jk}. \quad (29)$$

This allows us to isolate β_k in terms of C_{ijk} , specifically from the trace over C 's first two indices,

$$2 \sum_{i=j} C_{ijk} = \beta_k + \beta_k m - \beta_k = \beta_k m. \quad (30)$$

Hereafter we use $b_k = \beta_k/2 = \sum_{i=j} C_{ijk}/m$. Then with Eq. (29) the corresponding infinitesimal transformation is

$$\begin{aligned} f_i(\mathbf{x}) &= x_i + \sum_{jk} C_{ijk} x_j x_k \\ &= x_i + \sum_{jk} (b_j \delta_{ik} + b_k \delta_{ij} - b_i \delta_{jk}) x_j x_k \\ &= x_i + 2x_i \sum_j b_j x_j - b_i \sum_j (x_j)^2, \\ \mathbf{f}(\mathbf{x}) &= \mathbf{x} + 2(\mathbf{b} \cdot \mathbf{x})\mathbf{x} - \|\mathbf{x}\|^2 \mathbf{b}. \end{aligned} \quad (31)$$

We postpone the interpretation momentarily.

Thus we have found all continuously parameterizable infinitesimal conformal mappings connected to the identity and showed they come in four distinct types. By composing infinitely many such transformations, or "exponentiating" them, we obtain finite conformal mappings. Formally, this is the process of exponentiating the elements of a Lie algebra to obtain elements of a corresponding Lie group.

A.2 Finite Conformal Mappings

As an example of obtaining finite mappings from infinitesimal ones we take the infinitesimal rotations from Eq. (27) where we note that \mathbf{f} only deviates from the identity by an infinitesimal vector field $\mathbf{B}_{AS}\mathbf{x}$. By integrating the field we get the finite displacement of any point under many applications of \mathbf{f} , i.e. the integral curves $\mathbf{x}(t)$ defined by

$$\dot{\mathbf{x}}(t) = \mathbf{B}_{AS}\mathbf{x}(t), \quad \mathbf{x}(0) = \mathbf{x}_0. \quad (32)$$

This differential equation has the simple solution

$$\mathbf{x}(t) = \exp(t\mathbf{B}_{AS})\mathbf{x}_0. \quad (33)$$

Finally we recognize that when a matrix \mathbf{A} is antisymmetric, the matrix exponential $e^{\mathbf{A}}$ is orthogonal, showing that the finite transformation given by $t = 1$, $\mathbf{f}(\mathbf{x}_0) = \exp(\mathbf{B}_{AS})\mathbf{x}_0$, is indeed a rotation. Furthermore, it is intuitive that infinitesimal translations and scalings also compose into finite translations and scalings.

The infinitesimal transformation in Eq. (31) is non-linear in \mathbf{x} , so it does not exponentiate easily as for the other three cases. It helps to linearize with a change of coordinates $\mathbf{y} = \mathbf{x}/\|\mathbf{x}\|^2$ which happens to be an inversion:

$$\dot{\mathbf{x}}(t) = 2(\mathbf{b} \cdot \mathbf{x})\mathbf{x} - \|\mathbf{x}\|^2 \mathbf{b}, \quad (34)$$

$$\dot{\mathbf{y}}(t) = \frac{\dot{\mathbf{x}}}{\|\mathbf{x}\|^2} - 2 \frac{\mathbf{x} \cdot \dot{\mathbf{x}}}{\|\mathbf{x}\|^4} \mathbf{x} = -\mathbf{b}. \quad (35)$$

We now get the incredibly simple solution $\mathbf{y}(t) = \mathbf{y}_0 - t\mathbf{b}$, a translation, after which we can undo the inversion

$$\frac{\mathbf{x}(t)}{\|\mathbf{x}\|^2} = \frac{\mathbf{x}_0}{\|\mathbf{x}_0\|^2} - t\mathbf{b}. \quad (36)$$

This form is equivalent to a Special Conformal Transformation (SCT) [10], which we can see by defining the finite transformation as $\mathbf{f}(\mathbf{x}_0) = \mathbf{x}(1)$, and taking the inner product of both sides with themselves

$$\|\mathbf{f}(\mathbf{x}_0)\|^2 = \frac{\|\mathbf{x}_0\|^2}{1 - 2\mathbf{b} \cdot \mathbf{x}_0 + \|\mathbf{b}\|^2 \|\mathbf{x}_0\|^2}, \quad (37)$$

and finally isolating

$$\mathbf{f}(\mathbf{x}_0) = \frac{\|\mathbf{f}(\mathbf{x}_0)\|^2}{\|\mathbf{x}_0\|^2} \mathbf{x}_0 - \|\mathbf{f}(\mathbf{x}_0)\|^2 \mathbf{b} = \frac{\mathbf{x}_0 - \|\mathbf{x}_0\|^2 \mathbf{b}}{1 - 2\mathbf{b} \cdot \mathbf{x}_0 + \|\mathbf{b}\|^2 \|\mathbf{x}_0\|^2}. \quad (38)$$

In the process of this derivation we have learned that SCTs can be interpreted as an inversion, followed by a translation by $-\mathbf{b}$, followed by an inversion, and the infinitesimal Eq. (31) is recovered when the translation is small.

By composition, the four types of finite conformal mapping we have encountered, namely translations, rotations, scalings, and SCTs, generate the conformal group - the group of transformations of Euclidean space which locally preserve angles and orientation. The infinitesimal transformations we derived directly give the corresponding elements of the Lie algebra.

Eq. (11) also admits non-orientation preserving solutions which are not generated by the infinitesimal approach. Composing the scalings in Eq. (28) only produces finite scalings by a positive factor, i.e. $\mathbf{f}(\mathbf{x}) = e^\lambda \mathbf{x}$. Similarly, composing infinitesimal rotations does not generate reflections - non-orientation preserving orthogonal transformations that are not connected to the identity. The conformal group can be extended by including non-orientation preserving transformations, namely inversions, negative scalings, and reflections as in Table 1. All of these elements still satisfy Eq. (11), as do their closure under composition. By Liouville's theorem, these comprise all possible conformal mappings.

The important point for our discussion is that any conformal mapping can be built up from the simple elements in Table 1. In other words, a neural network can learn any conformal mapping by learning a sequence of the simple elements.

A.3 Conformal Embeddings

Whereas conformal mappings have been exhaustively classified, conformal embeddings have not. While the defining equations for a conformal embedding $\mathbf{g} : \mathcal{U} \rightarrow \mathcal{X}$, namely

$$\mathbf{J}_{\mathbf{g}}^T(\mathbf{u}) \mathbf{J}_{\mathbf{g}}(\mathbf{u}) = \lambda^2(\mathbf{u}) \mathbf{I}_m, \quad (39)$$

appear similar to those of conformal mappings, we cannot apply the techniques from Apps. A.1 and A.2 to enumerate them. Conformal embeddings do not necessarily have identical domain and codomain. As such, finite conformal embeddings can not be generated by exponentiating infinitesimals.

The lack of full characterization of conformal embeddings hints that they are a richer class of functions. For a more concrete understanding, we can study Eq. (39) as a system of PDEs. This system consists of $m(m+1)/2$ independent equations (noting the symmetry of $\mathbf{J}_{\mathbf{g}}^T \mathbf{J}_{\mathbf{g}}$) to be satisfied by $n+1$ functions, namely $\mathbf{g}(\mathbf{u})$ and $\lambda(\mathbf{u})$. In the typical case that $n < m(m+1)/2 - 1$, i.e. n is not significantly larger than m , the system is overdetermined. Despite this, solutions do exist. We have already seen that the most restricted case $n = m$ of conformal mappings admits four qualitatively different classes of solutions. These remain solutions when $n > m$ simply by having \mathbf{g} map to a constant in the extra $n - m$ dimensions.

Intuitively, adding an extra dimension for solving the PDEs is similar to introducing a slack variable in an optimization problem. In case it is not clear that adding additional functions $\mathbf{g}_i, i > m$ enlarges the class of solutions of Eq. (39), we provide a concrete example. Take the case $n = m = 2$ for a

fixed $\lambda(u_1, u_2)$. The system of equations that $\mathbf{g}(\mathbf{u})$ must solve is

$$\begin{aligned}\left(\frac{\partial g_1}{\partial u_1}\right)^2 + \left(\frac{\partial g_2}{\partial u_1}\right)^2 &= \lambda^2(u_1, u_2), \\ \left(\frac{\partial g_1}{\partial u_2}\right)^2 + \left(\frac{\partial g_2}{\partial u_2}\right)^2 &= \lambda^2(u_1, u_2), \\ \frac{\partial g_1}{\partial u_1} \frac{\partial g_1}{\partial u_2} + \frac{\partial g_2}{\partial u_1} \frac{\partial g_2}{\partial u_2} &= 0.\end{aligned}\tag{40}$$

Suppose that for the given $\lambda(u_1, u_2)$ no complete solution exists, but we do have a $\mathbf{g}(\mathbf{u})$ which simultaneously solves all but the first equation. Enlarging the codomain \mathcal{X} with an additional dimension ($n = 3$) gives an additional function $g_3(\mathbf{u})$ to work with while $\lambda(u_1, u_2)$ is unchanged. The system of equations becomes

$$\begin{aligned}\left(\frac{\partial g_1}{\partial u_1}\right)^2 + \left(\frac{\partial g_2}{\partial u_1}\right)^2 + \left(\frac{\partial g_3}{\partial u_1}\right)^2 &= \lambda^2(u_1, u_2), \\ \left(\frac{\partial g_1}{\partial u_2}\right)^2 + \left(\frac{\partial g_2}{\partial u_2}\right)^2 + \left(\frac{\partial g_3}{\partial u_2}\right)^2 &= \lambda^2(u_1, u_2), \\ \frac{\partial g_1}{\partial u_1} \frac{\partial g_1}{\partial u_2} + \frac{\partial g_2}{\partial u_1} \frac{\partial g_2}{\partial u_2} + \frac{\partial g_3}{\partial u_1} \frac{\partial g_3}{\partial u_2} &= 0.\end{aligned}\tag{41}$$

Our partial solution can be worked into an actual solution by letting g_3 satisfy

$$\left(\frac{\partial g_3}{\partial u_1}\right)^2 = \lambda^2(u_1, u_2) - \left(\frac{\partial g_1}{\partial u_1}\right)^2 - \left(\frac{\partial g_2}{\partial u_1}\right)^2,\tag{42}$$

with all other derivatives of g_3 vanishing. Hence g_3 is constant in all directions except the u_1 direction so that, geometrically speaking, the u_1 direction is bent and warped by the embedding into the additional x_3 dimension.

To summarize, compared to conformal mappings, with dimension-changing conformal embeddings the number of equations in the system remains the same but the number of functions available to satisfy them increases. This allows conformal embeddings to be much more expressive than the fixed set of conformal mappings, but also prevents an explicit classification and parameterization of all conformal embeddings.

B Experimental Details

B.1 Synthetic Spherical Distribution

Model The injective part of the model \mathbf{g} was composed of a padding layer, SCT, orthogonal transformation, and translation (See App. A.2 for the definition of SCT). The bijective part \mathbf{h} stacked three sets of Glow-style blocks, each having an ActNorm, Invertible 1×1 Convolution, and Affine Coupling layer.

Training We trained the reconstruction loss with a 100-epoch manifold-warmup phase for \mathbf{g} , then trained the mixed loss function in Eq. (7) with the end-to-end log-likelihood for 100 epochs, and finally 100 epochs with the manifold model fixed to fine-tune the density. We used a batch size of 100 and a learning rate of 1×10^{-3} .

Data For illustrative purposes we generated a synthetic dataset from a known distribution on a spherical surface embedded in \mathbb{R}^3 . The sphere is a natural manifold with which to demonstrate learning a conformal embedding with a CEF, since we can analytically find suitable maps $\mathbf{g} : \mathbb{R}^2 \rightarrow \mathbb{R}^3$ that embed the sphere⁶ with Cartesian coordinates describing both spaces. For instance consider

$$\mathbf{g} = \left(\frac{2r^2 z_1}{z_1^2 + z_2^2 + r^2}, \frac{2r^2 z_2}{z_1^2 + z_2^2 + r^2}, r \frac{z_1^2 + z_2^2 - r^2}{z_1^2 + z_2^2 + r^2} \right),\tag{43}$$

⁶Technically the “north pole” of the sphere $(0, 0, 1)$ is not in the range of \mathbf{g} , which leaves a manifold $\mathbb{S}^2 \setminus \{\text{north pole}\}$ that is topologically equivalent to \mathbb{R}^2 .

where $r \in \mathbb{R}$ is a parameter. Geometrically, this embedding takes the domain manifold, viewed as the surface $x_3 = 0$ in \mathbb{R}^3 , and bends it into a sphere of radius r centered at the origin. Computing the Jacobian directly gives

$$\mathbf{J}_{\mathbf{g}}^T \mathbf{J}_{\mathbf{g}} = \frac{4r^4}{(z_1^2 + z_2^2 + r^2)^2} \mathbf{I}_2, \quad (44)$$

which shows that \mathbf{g} is a conformal embedding (Eq. (5)) with $\lambda(\mathbf{z}) = \frac{2r^2}{z_1^2 + z_2^2 + r^2}$. Of course, this \mathbf{g} is also known as a *stereographic projection*, but here we view its codomain as all of \mathbb{R}^3 , rather than the 2-sphere.

With this in mind it is not surprising that a CEF can learn an embedding of the sphere, but we would still like to study how a density confined to the sphere is learned. Starting with a multivariate Normal $\mathcal{N}(\boldsymbol{\mu}, \mathbf{I}_3)$ in three dimensions we drew samples and projected them radially onto the unit sphere. This mimics the much more complicated distribution given by integrating out the radial coordinate from the standard Normal distribution

$$p_{\mathcal{M}}(\phi, \theta) = \int_0^\infty \frac{1}{(2\pi)^{3/2}} \exp \left\{ -\frac{1}{2} (r^2 - 2r (\cos \phi \sin \theta, \sin \phi \sin \theta, \cos \theta) \cdot \boldsymbol{\mu} + \|\boldsymbol{\mu}\|^2) \right\} r^2 dr. \quad (45)$$

With the shorthand $\mathbf{t} = (\cos \phi \sin \theta, \sin \phi \sin \theta, \cos \theta)$ for the angular direction vector, the integration can be performed

$$p_{\mathcal{M}}(\phi, \theta) = \frac{1}{2^{5/2} \pi^{3/2}} e^{-\|\boldsymbol{\mu}\|^2/2} \left(2\mathbf{t} \cdot \boldsymbol{\mu} + \sqrt{2\pi} ((\mathbf{t} \cdot \boldsymbol{\mu})^2 + 1) e^{(\mathbf{t} \cdot \boldsymbol{\mu})^2/2} \left(\operatorname{erf} \left(\mathbf{t} \cdot \boldsymbol{\mu} / \sqrt{2} \right) + 1 \right) \right). \quad (46)$$

This distribution is visualized in Fig. 2 for the parameter $\boldsymbol{\mu} = (-1, -1, 0)$.

B.2 CelebA

Models The baseline’s embedding \mathbf{g} is a Glow-style network of 3 levels and 2 steps per level: the output of each scale is reshaped into 8×8 , and all scales are concatenated. We then apply an invertible 1×1 convolution, and project the input down to 1536 dimensions. Since this network is not conformal, joint training is intractable, so it must be trained sequentially.

On the other hand, both CEFs use the same conformal architecture for \mathbf{g} . The basic architecture follows. Between every layer, trainable scaling and shift operations were applied.

$$\begin{aligned} \mathbf{x} \ (3 \times 64 \times 64) &\rightarrow 4 \times 4 \text{ Householder Conv} \\ &\rightarrow 1 \times 1 \text{ Householder Conv} \\ &\rightarrow 1 \times 1 \text{ Conditional Orthogonal Conv} \\ &\rightarrow \text{Pad Channels}(48, 24) \\ &\rightarrow 2 \times 2 \text{ Householder Conv} \\ &\rightarrow 1 \times 1 \text{ Householder Conv} \\ &\rightarrow 1 \times 1 \text{ Conditional Orthogonal Conv} \\ &\rightarrow \text{Pad Channels}(96, 48) \\ &\rightarrow 2 \times 2 \text{ Householder Conv} \\ &\rightarrow 1 \times 1 \text{ Householder Conv} \\ &\rightarrow 1 \times 1 \text{ Conditional Orthogonal Conv} \\ &\rightarrow \text{Pad Channels}(192, 96) \\ &\rightarrow \mathbf{u} \ (96 \times 8 \times 8) \end{aligned}$$

Training For the sequential baseline and sequential CEF, \mathbf{g} was trained with a reconstruction loss in a 10-epoch manifold-warmup phase, and then \mathbf{h} was trained to maximize likelihood for 100-epochs. The joint CEF was trained with a 10-epoch manifold warmup phase, and then the mixed loss function in Eq. (7) was optimized for 100 epochs with weights of 0.001 for the likelihood and 100 for the reconstruction loss.

All models were trained with the Adam optimizer [24] with learning rate 1×10^{-5} and a batch size of 32. Using a single NVIDIA TITAN V, the sequential baseline and sequential CEF ran for 34 hours, while the joint CEF ran for 65 hours.